




# Properties of Casting Al-Cu Alloy Modified by Mixed Rare Earth (La, Ce) and its Mechanism Analyzed

Xin Li <sup>a</sup>, Medetbek Uulu Nurtilik <sup>a</sup>, Qi Zeng <sup>b</sup>, Ziqi Zhang <sup>a</sup>, Lixia Wang <sup>a</sup>,  
Quan Wu <sup>a</sup>, Peixuan Mao <sup>a</sup>, Rong Li <sup>a,\*</sup> 

<sup>a</sup> School of Mechanical & Electrical Engineering, Guizhou Normal University, China

<sup>b</sup> Guiyang Huaheng Mechanical Manufacture CO.LTD, China

\* Correspondence contact: e-mail: lirong9242001@163.com

Received 09.11.2023; accepted in revised form 19.03.2024; available online 05.06.2024

## Abstract

To improve the mechanical properties of casting aluminum-copper alloy, the mixed rare earth (RE) was added to ZL206 and its properties and the enhanced mechanism of alloy were researched. The results showed that the strength and hardness of the composite were improved by 10.2% and 6.2%, respectively. After adding mixed RE, which was led by the heterogeneous enrichment area blocking the growth of the  $\alpha$ -Al phase and making grain refinement during the solidification process. The simulation results of RE surface adsorption models by first principles also showed that the elastic constant calculation improved the bulk modulus, shear modulus, and Young's modulus of the material. The addition of mixed RE enhances the strength and hardness, although it adversely affects toughness and reduces the machining index. Also, the work function decreased, and the Fermi level increased, reflecting that the electron locality on each band was strong and the bonding state of the alloy system was covalent, which showed that the corrosion resistance was enhanced after adding mixed RE. It provides a new method for the mechanism of RE-modified aluminum-copper alloys and expands the direction of cast aluminum-copper alloy modification.

**Keywords:** Cast aluminum alloy, Mechanical properties, RE modification, Simulation calculation, Mechanism analysis

## 1. Introduction

Casting aluminum-copper alloy has the advantages of low density, high specific strength, and high specific stiffness, which was widely used in vehicle engineering, aerospace, military equipment, and other fields, occupying an irreplaceable position in the lightweight production of complex internal cavity parts [1, 2]. However, aluminum alloy has low surface hardness and weak mechanical resistance, so its application field cannot be expanded in a broader range. Nowadays, many scholars try to obtain casting aluminum alloys with excellent properties by optimizing alloy

formulas, improving the heat treatment process [3-5], optimizing processing technology [6, 7], and other methods. Modifying by adding active rare earth metal (RE) elements is a hot spot in current research.

Regarding rare earth optimization alloy formulation, scholars have analyzed the effect of adding elements on the properties of the alloy by using experimental and simulation methods. Researchers have found that rare earth elements located in the third subgroup of the periodic table have particular 4f subaltern layer electrons, active chemical properties, low binding energy, and easy to react with external elements [8], and quickly form precipitated phases with high thermal stability with Al, Cu, Mg and other elements [9-12].



Shikun [13, 14] studied the effects of adding Ce with a mass fraction from 0 to 6wt.% on the solidification zone, solidification volume change, hot cracking tendency, and casting structure of Al-4.5Cu alloy. It was pointed out that the casting performance was significantly improved after the addition of 4wt.% Ce. Below [15] used the element Ce to develop creep-resistant aluminum alloys and transition metals with high and low solubility, and his research results showed that aluminum solid solutions should be used. An alloy containing soluble transition metals (Zr, Mn, and Cr) and a second phase containing low soluble transition metals (Fe, Ni, Ce) results in an optimal combination of creep strength and casting properties. In addition, Nikolay A [16] carried out related research on alloys of the Al-Ce-Ni system, and the results showed that the Al-Ce-Ni ternary eutectic system (12wt.%Ce, 6wt.%Ni) showed good mechanical properties and excellent casting properties at room temperature and high temperature. The above studies verified the metamorphic effect of rare earth elements on aluminum alloys by experimental means. However, the deeper mechanism of action has not been explored, and the microstructural changes in the process of alloy property changes have not been explored, and the results have only been recorded from a macroscopic point of view. Although the above studies have guided the production practice, it is no doubt that there is still room for improvement.

With the development of material calculation theory, the calculation of properties of aluminum alloy modified by adding rare earth has become more and more thorough. First-principles calculations, a simulation research method based on density functional theory, were more widely applied in materials research [17, 18]. Just as Yan, Yue, et al. [19, 20] studied the mechanism of Ce modifying the photoelectric properties and electronic structures of SiO<sub>2</sub> and ZnO, The results show that the excitation energy of plasma is reduced by the introduction of Ce element, indicating that Ce doping is an effective strategy to improve the optical properties of SiO<sub>2</sub>. Zhang, Y.Huang [21-23] calculated the electronic structure, elastic constants, and mechanical properties of Al<sub>2</sub>Cu and Al<sub>2</sub>CuMg, two typical precipitates in Al-Cu-Mg alloys. The results show that the Al<sub>2</sub>Cu phase has higher electronic structure stability and better mechanical properties as a strengthening phase in Al-Cu alloys. Based on the calculation of the surface adsorption model, P.Cornette et al. [24] found that the Al<sub>2</sub>Cu (001) surface exhibited higher work function and stronger corrosion resistance in the adsorption behavior of aluminum alloy surface. The application of first principles fills the gap in the microscopic study of aluminum alloy modification. However, the traditional first-principles

research is used to analyzing the internal changes of alloys with a series of numerical simulation results, which needs more practical proof, so it is necessary to add physical verification experiments to the research process.

In order to get the high performance aluminum alloys, it is not only necessary to carry out experimental verification studies but also to analyze the mechanism of adding alloying elements to the material modification. This study is based on the performance of casting aluminum-copper alloy ZL206 after adding rare earth (La, Ce). ZL206 is mainly used in the production field of medium-sized castings, which require high rigidity, static solid load capacity, and small deformation. The changes in strength, hardness and plasticity before and after adding rare earth were measured, and the metallographic structure and fracture morphology were observed. Then, the Al<sub>2</sub>Cu (001) surface model and the surface growth stacking model before and after the adsorption of mixed RE was established, and the model energy changes before and after the adsorption of mixed RE were analyzed for the stability of different adsorption modes and adsorption sites. The effects of mixed RE on the properties of cast aluminum-copper alloys are also reflected by the work function and elastic constants. Finally, the internal mechanism of mixed RE modified casting aluminum-copper alloy was explored by combining the experimental and calculation results. Compared to traditional research methods, this study combined the advantages of first-principles simulation and physical experiments. It carried out research and analysis from a dual perspective, found the bridge of communication between micro and macro phenomena. It is expected to find the essence of the mechanism of rare earth modified aluminum alloys.

## 2. Experiment

### 2.1. Experimental material composition, preparation process and testing methods

Al-8Cu-2Re-Mn aluminum-copper alloy (ZL206) was prepared, and its chemical element composition is shown in Table 1 [25]. The Al-La-Ce intermediate alloy containing a certain mass fraction of rare earth elements as a strengthening additive, and the intermediate alloy composition is shown in Table 2.

Table 1.

Chemical element composition and content of Al-8Cu-2Re-Mn aluminum copper alloy (ZL206) (wt.%)

| Element | Cu      | Mn      | Re      | Zn    | Zr       | Fe     | Others | Al        |
|---------|---------|---------|---------|-------|----------|--------|--------|-----------|
| Content | 7.6-8.4 | 0.7-1.1 | 1.5-2.3 | 0-0.4 | 0.1-0.25 | 0-0.25 | 0-0.15 | allowance |

Table 2.

Chemical element composition and content of Al-La-Ce intermediate alloy (wt.%)

| Element | La   | Ce  | Fe   | Si   | Al        |
|---------|------|-----|------|------|-----------|
| Content | 5.19 | 4.7 | 0.06 | 0.05 | allowance |

The preparation process was as follows: the material of the ZL206 alloy was just like the aluminum ingots (99.99wt.%,

Yunnan Al Co. LTD), copper rods (T2, 99.5wt%), Al-Zn intermediate alloy (10wt%, Chongqin Shunbo), Al-Zr intermediate

alloy (4.65wt%, Chongqin Shunbo) were added and melted in a graphite crucible. After the melt was prepared, the Mn was added by agent (75wt%, Yunnan Al Co. LTD) was pressed into the melt. And then, a motor agitator is used to stir the melt. The alloy without the addition of rare earth needed to be insulated by a nitrogen atmosphere for refining, slag removal and standing for 20 minutes before pouring the test rod. For the alloy liquid with rare earths, the temperature of the aluminum liquid needs to be reduced to about 600°C and then the Al-La-Ce intermediate alloy (alloy element was shown in Table 2) was added. After the Al-La-Ce intermediate alloy was completely melted, the crucible temperature was raised

to about 750°C and stirred with a motor agitator. After that, the refining, slag removal and pouring steps were repeated as for the normal alloy. Both different metal liquids were poured into the mold that had been preheated to 200-300°C, the target test rod was obtained after 5 minutes of air cooling. The main elements of rare earth modified alloy are shown in Table 3. The group containing rare earths is named Group A, while the group without rare earths is named Group B. The outline and dimensions of the test bars are shown in Fig. 1, which was satisfied with the Chinese standard GB/T228-2002 [26].

Table 3. Element composition and content of real casting ZL206 (wt.%)

| Element | Cu  | Mn   | Zn  | Zr  | La  | Ce  | Others | Al        |
|---------|-----|------|-----|-----|-----|-----|--------|-----------|
| Content | 8.0 | 0.85 | 0.3 | 0.2 | 1.0 | 1.0 | 0.02   | allowance |

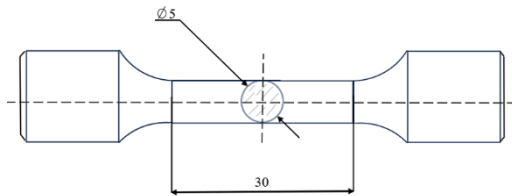


Fig. 1. Outline and dimensions of test bars

Finally, experiments were conducted to investigate the tensile strength, elongation, hardness, metallographic structure, and fracture morphology of the two groups of test rods, and a series of data were collected for analysis. The tensile strength and elongation were tested by a testing machine (WAW-300). The hardness was tested by an HBRVU-187.5 Optical Bloyev hardness tester. The metallographic structure before and after corrosion (Etching solution formula: 5mlHF+25mlHNO<sub>3</sub>+30mlH<sub>2</sub>O) was recorded by 4XC-MS metallographic microscope. The fracture morphology of the sample was recorded by scanning electron microscope (Sigma 300).

## 2.2. Calculation model construction

### 2.2.1. Model construction

The Visualizer module of Materials Studio 2020 software was used to build the simulation calculation model of this study. As shown in Fig.2 (a), the adsorbent of the adsorption model is the La-Ce molecule, La atom, and Ce atom. The adsorption substrate is shown in Fig.2 (b), the space group of Al<sub>2</sub>Cu is P4/mmm[26] belonging to the tetragonal-crystal system, and the lattice constants are:  $a=b=4.10518 \text{ \AA}$ ,  $c=2.89131 \text{ \AA}$ ,  $\alpha=\beta=\gamma=90^\circ$ ,  $V=48.7259 \text{ \AA}^3$ . The axial growth surface of Al<sub>2</sub>Cu (001) was selected as the adsorption surface. The selection was based on previous conclusions. P.Cornette [24] found that the surface of Al<sub>2</sub>Cu (001) has higher work function and stronger corrosion resistance, so the

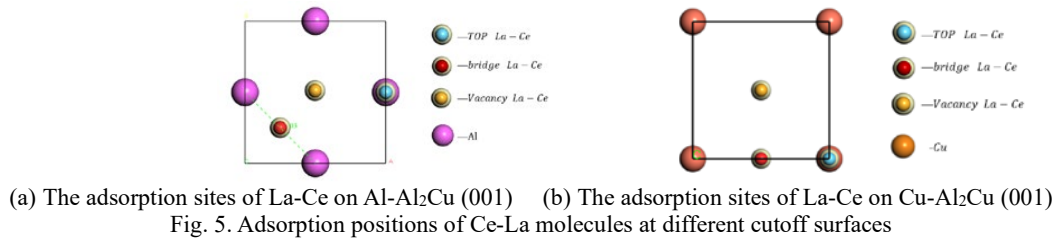
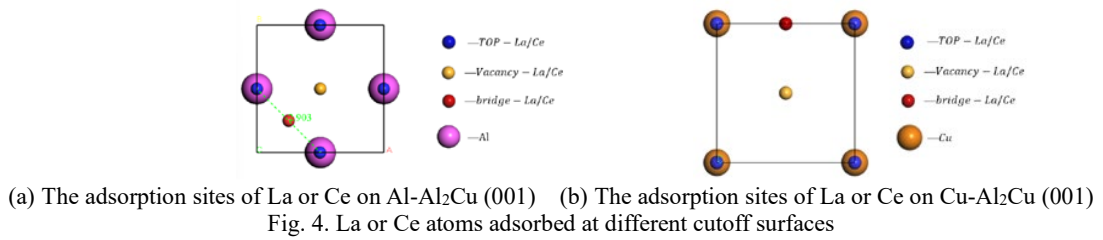
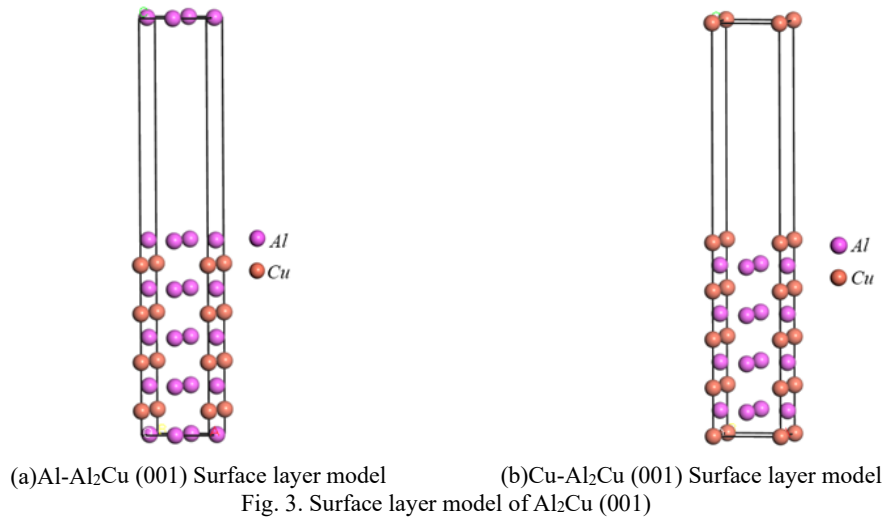
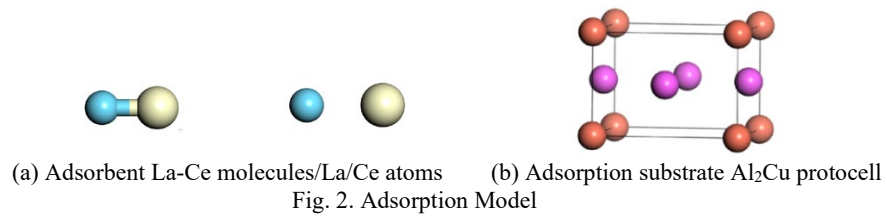
surface of Al<sub>2</sub>Cu (001) was selected in this study. The Al<sub>2</sub>Cu (001) surface is a polar surface, according to the different types of polar surface atoms, the Al<sub>2</sub>Cu (001) surface can be divided into two cutoff modes: Al-Al<sub>2</sub>Cu and Cu-Al<sub>2</sub>Cu, as shown in Fig.3 (a) and (b).

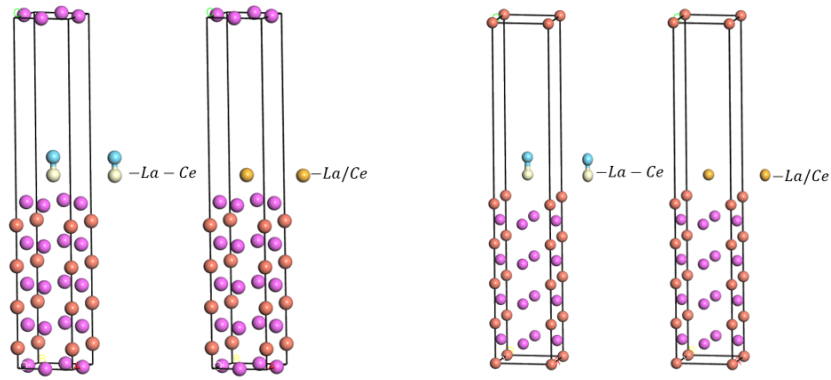
In order to maximize the simulation of the actual surface adsorption state, a series of models were built to simulate the adsorption states of three adsorption substances. The La atom, Ce atom, and La-Ce compounds are respectively adsorbed at different positions on two cutoff surfaces of Al<sub>2</sub>Cu (001).

Fig.4 (a) and (b) show the highly symmetric adsorption positions of La and Ce atoms on the two cutoff surfaces, namely the top (T), bridge (B), and vacancy (V), respectively. The tiny atoms represent the La and Ce atoms, and the large atoms are the surface atoms to be adsorbed. Fig.5 (a) and (b) show the highly symmetric adsorption positions of La-Ce molecules on the two cutoff surfaces. The two stacked atoms represent La-Ce molecules, the large atom representing the adsorbed surface atom.

The adsorption models of different cutoff surfaces are shown in Fig.6 (a). It illustrates two adsorption modes of each adsorbent on the Al-Al<sub>2</sub>Cu (001) surface. The left model in Fig.6 (a) represents the adsorption of the La-Ce compound, while the right model depicts the adsorption of La or Ce elements as free atoms on the surface. Fig. 6 (b) demonstrates the behavior of various adsorbents on Cu-Al<sub>2</sub>Cu (001). Both models are shown with the adsorption site vacancy (V) as an example.

Based on the above operation, the adsorption model of 18 kinds of mixed rare earth (La, Ce, La-Ce) on the surface of Al<sub>2</sub>Cu (001) was established. In the model, the number of atomic layers of the adsorption base is 9, the thickness of the vacuum layer is 10 Å, the middle three layers of the adsorption base are fixed, and the upper and lower three layers are used for surface relaxation. The length of the La-Al bond is 1.95 Å, the La-Cu bond is 2.05 Å, the Ce-Al bond is 1.75 Å, and the Ce-Cu bond is 1.85 Å.





(a) Different adsorption modes of Al-Al<sub>2</sub>Cu (001) (B) Different adsorption modes of Cu-Al<sub>2</sub>Cu (001)  
 Fig. 6. Adsorption states of various adsorbents at different cutoff surfaces

### 2.2.2. Calculation method

The simulation calculations in this study were performed using the Vienna Ab initio Simulation Package (VASP) [27, 28], based on the first-principles method of density functional theory (DFT). The interaction between nuclei and valence electrons was described using the Projector Augmented Wave (PAW) method, and the electron wave function was developed using the plane wave group method. The exchange correlation between electrons was processed using PBE functional under generalized gradient approximation (GGA) [29], with all *K*-points in the Brillouin region taken as 8×8×1. Valence shell electron configuration is Al-3s<sup>2</sup>3p<sup>1</sup>, Cu-3d<sup>10</sup>4s<sup>1</sup>, La-5d<sup>1</sup>6s<sup>2</sup>, Ce-4f<sup>1</sup>5d<sup>1</sup>6s<sup>2</sup>. After conducting a convergence test, the plane wave truncation energy was determined to be 600 eV. The self-consistent cycle (SCF) was used to solve the Kohn-Sham equation. The energy convergence value was set at 1×10<sup>-5</sup> eV/atom, and force convergence was controlled within -0.01 eV/nm. Additionally, traditional methods showed significant deviation for the outer orbits of La and Ce elements; hence, this research employed the DFT+U method to correct calculation results. The Hubbard *U* value for La/Ce elements is 6.0 eV [30, 31], while the *J* value remains at 0 eV.

#### (1) Work function and adsorption energy

Calculation of adsorption energy: In the simulation calculation, the structure of the established adsorption model is first optimized to ensure that the crystal cell is in its ground state. Subsequently, the energies of the adsorbent and adsorption substrate are calculated individually before and after they combined different adsorption sites on the Al<sub>2</sub>Cu (001) surface. The equation (1) is then employed to determine the adsorption energy of mixed rare earth elements (La, Ce) on the surface of Al<sub>2</sub>Cu (001) [32]. In equation (1),  $E_{ad}$  represents the adsorption energy,  $E_{X/as}$  denotes the total energy of the surface model after adsorption where X=Al/Cu signifies either an aluminum cutoff surface or a copper cutoff surface respectively, and  $E_{as}$  represents the energy of an individual Adsorbed substance. When  $X/as = Al-La-Ce$ ,  $E_{X/as}$  represents the total energy of La-Ce molecules adsorbed to the Al cutoff surface, And so it goes for other models. Lastly,  $E_X$  is the energy of the surface model of the adsorption substrate Al<sub>2</sub>Cu (001).

$$E_{ad} = E_{X/as} - E_{as} - E_X \quad (1)$$

The electron work function is defined as the minimum energy required for electrons to escape from the interior of a solid material to the surface of a solid [33]. It is also defined as the minimum work required for an electron to escape from the Fermi level to the vacuum level. The results show that the electron work function is closely related to the corrosion potential and can be used as a sensitive parameter to study the corrosion wear mechanism. This parameter reflects the corrosion tendency of the material itself and can be calculated by equation (2) [34].

$$W_{x/as} = E_{vac} - E_F \quad (2)$$

In the equation (2),  $W_{x/as}$  represents the electronic work function after adsorption of the Al<sub>2</sub>Cu (001) plane by mixed RE adsorbent.  $E_{vac}$  denotes the vacuum energy level of the material, and  $E_F$  is its Fermi energy level. To gain an intuitive understanding of how La and Ce adsorption on the surface affects the material's work function, we calculated the difference in work function before and after adsorption for analysis, as shown in equation (3).

$$\Delta W = W_{X-Al_2Cu} - W_{as} \quad (3)$$

In equation (3),  $\Delta W$  represents the difference in work function before and after the adsorption of each surface model, while  $W_{X-Al_2Cu}$  denotes the electronic work function of the adsorption base. There are two different cutoff surfaces:  $W_{Al-Al_2Cu} = 4.12$  when X=Al, and  $W_{Cu-Al_2Cu} = 4.23$  when X=Cu. Compared with the value calculated by previous researchers[36],  $W_{Al_2Cu} = 4.10$ , the error is insignificant, and thus the calculated results are considered reliable.

Fig.7 is an example of calculating the electronic work function on the surface of Al<sub>2</sub>Cu (001) without adsorption. *Z* on the X-axis represents the vertical height of the material surface, and *V* on the Y-axis represents electrostatic potential energy. The interval closer to the surface can be observed to exhibit periodic changes in electrostatic potential energy, which is due to the regular arrangement of electrons in the surface layer of the material. In the vacuum region away from the surface, the energy curve converges

because no electrons are present. The platform value corresponds to the value of the electron work function when the Fermi level is zero on the  $Y$ -axis.

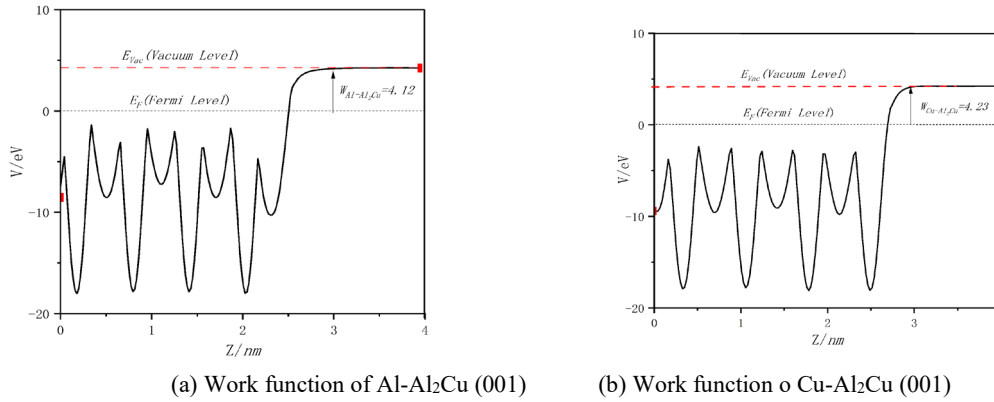


Fig. 7. Diagram of Work Function Calculation

## (2) Elastic constant and mechanical properties

The elastic constant describes the stiffness of the crystal in response to the applied strain  $\varepsilon$ . When the strain is slight, the internal energy of the system is related to the strain in a quadratic linear way. Based on this energy strain relation, the relation between stress and strain can be obtained by loading the strain in different directions and sizes of the crystal, and the elastic constant of the crystal can finally be converted.

$\text{Al}_2\text{Cu}$  crystal belongs to the tetragonal system and has six independent elastic constants  $C_{ij}$ , ( $C_{11}$ ,  $C_{12}$ ,  $C_{13}$ ,  $C_{33}$ ,  $C_{44}$ ,  $C_{66}$ ).

According to the requirements of Born mechanical stability conditions, the elastic constants can be used as the basis for judging the mechanical stability of intermetallic compounds. The stability standard of the tetragonal system is  $C_{11} > 0$ ,  $C_{33} > 0$ ,  $C_{66} > 0$ ,  $C_{44} > 0$ ,  $C_{11} - C_{12} > 0$ ,  $C_{11} + C_{33} - 2C_{13} > 0$ ,  $2C_{11} + 2C_{12} + C_{33} + 4C_{13} > 0$  [36]. Only crystals with elastic constants meeting the above standards can exist statically. The calculated results of elastic constant of this study in Table 4 are basically the same as the calculated results of reference [37]. It means this the calculation method is reliable. Then, the elastic constants of other adsorption models after geometric optimization were calculated.

Table 4. Comparison of the calculated results in this study with those in the references

| Calculated object | $C_{11}$ / (GPa) | $C_{12}$ / (GPa) | $C_{13}$ / (GPa) | $C_{33}$ / (GPa) | $C_{44}$ / (GPa) | $C_{66}$ / (GPa) |
|-------------------|------------------|------------------|------------------|------------------|------------------|------------------|
| References [37]   | 185.0            | 12.0             | 68.0             | 142.0            | 51.0             | 38.0             |
| This study        | 189.5            | 12.2             | 70.0             | 136.4            | 58.7             | 53.3             |

The elastic properties of materials directly related to elastic constants can be represented by bulk modulus  $B$ , shear modulus  $G$ , Young's modulus  $E$ , and Poisson's ratio  $\nu$ . The volume modulus  $B$  and shear modulus  $G$  can be obtained by Voigt Reuss Hill approximation, and the calculation method is shown in equations (4)-(8) [38].

$$B_v = B_R = \frac{C_{11} + 2C_{12}}{3} \quad (4)$$

$$G_v = \frac{3C_{44} + C_{11} - C_{12}}{5} \quad (5)$$

$$G_R = \frac{5C_{44} (C_{11} - C_{12})}{4C_{44} + 3 (C_{11} - C_{12})} \quad (6)$$

$$B = \frac{B_v + B_R}{2} \quad (7)$$

$$G = \frac{G_v + G_R}{2} \quad (8)$$

In the equations 4-8,  $B_v$ ,  $G_v$ ,  $B_R$ ,  $G_R$ ,  $B$ ,  $G$ , and others are calculated using the Voigt, Reuss, and Hill methods for bulk modulus and shear modulus, respectively. There are also Young's modulus  $E$  and Poisson's ratio  $\nu$  associated with parameters  $B$  and  $G$ . The calculation method is shown in the following equations 9 and 10 [36].

$$E = \frac{9BG}{3B+G} \quad (9)$$

$$\nu = \frac{3B-2G}{2(3B+G)} \quad (10)$$

The bulk modulus and Young's modulus can evaluate the ability of the material to resist deformation under stable pressure. The higher the value, the better the stiffness of the material, and the less elastic deformation will occur.  $G$  and  $\nu$  are often used to measure the ability of a material to resist shear deformation. The greater the values, the better the plasticity of the material. The change in ductility and tough-brittleness of the material can also be predicted by a general criterion introduced by Pugh [38]. That is,

when the ratio  $B/G$  of the bulk modulus  $B$  to the shear modulus  $G$  is more significant than 1.75, the material shows plasticity. otherwise, it is brittle. The greater the ratio, the better the plasticity[39].

In equation (11),  $H_V$  represents the predicted Vickers hardness theory value of the material, which was calculated by Candan et al. [40] based on a new theoretical model proposed by Pugh modulus ratio  $k=G/B$  [38]. It can be calculated by equation (11). The changing trend of  $H_V$  indirectly reflects the performance changes of the calculated material.

$$H_V = 2 (k^2 G)^{0.585} - 3 \quad (11)$$

Sun et al. [41] proposed a theoretical model to predict mechanical properties of materials based on elastic constants, and the calculated result value was called machining index  $u_M$ . It can be calculated by equation (12), The higher the value, the better the material's machinability. For metal materials, the production not only puts forward the requirements on the material's performance but also needs good process performance, and excellent

machinability significantly improves the scope of application of the material.

$$u_M = B/C_{44} \quad (12)$$

### 3. Result analysis

#### 3.1. Analysis of mechanical property results

Table 5 shows the results of three kinds of mechanical properties of composite materials under the experimental design. In order to reduce the error caused by the experiment, three samples are taken for mechanical property testing. The experimental groups 1-3 are three samples of Al-8Cu-2Re-Mn alloy, while the samples of Al-8Cu-2Re-Mn-0.5La-0.5Ce alloy after adding Al-La-Ce are groups 4-6.

Table 5. Mechanical properties of composites before and after al La, Ce addition

| Experimental group number | Strength (MPa) | Average value (MPa) | Standard Deviation | Hardness (HV) | Average value (HV) | Standard deviation | Elongation rate $\Delta$ (%) | Average value $\Delta$ (%) | Standard deviation |
|---------------------------|----------------|---------------------|--------------------|---------------|--------------------|--------------------|------------------------------|----------------------------|--------------------|
| 1                         | 185            |                     |                    | 83.7          |                    |                    | 4.6                          |                            |                    |
| 2                         | 193            | 189                 | 3.27               | 82.5          | 84.5               | 2.04               | 3.3                          | 4.3                        | 0.64               |
| 3                         | 189            |                     |                    | 87.3          |                    |                    | 4.7                          |                            |                    |
| 4                         | 199            |                     |                    | 95.1          |                    |                    | 3.3                          |                            |                    |
| 5                         | 213            | 211                 | 9.09               | 98.5          | 97.2               | 1.50               | 2.7                          | 2.9                        | 0.28               |
| 6                         | 221            |                     |                    | 98.0          |                    |                    | 2.7                          |                            |                    |

As can be seen from Table 5, the strength and hardness of Al-8Cu-2Re-Mn-La-Ce alloy are significantly improved after the addition of Al-La-Ce, while the elongation of Al-8Cu-2Re-Mn alloy is decreased. According to the average value of the data in Table 5, the strength and hardness of the composite material after adding Al-La-Ce are 211 MPa and 97.2 HV, which are respectively increased by 11.6% and 15%(189 MPa and 84.5 HV) compared with the original alloy material. Elongation is 2.9%, 33% lower than 4.3% of the raw material alloy. ZL 206 requires an external force to push out the work parts during the release process of casting. If the plastic deformation performance is good, which means the part will be easy to deform in the process of ejecting the workpiece, resulting in the shape and size of the workpiece changing. On the whole, adding mixed rare earth (La-Ce) is beneficial to improve the mechanical properties of cast aluminum

alloy Al-5Cu-Mn, especially in terms of strength and hardness, but the elongation is somewhat reduced.

#### 3.2. Analysis of microstructure results

##### 3.2.1. Metallographic structure

Fig. 8. shows the raw material of Al-8Cu-2Re-Mn and the composite material of Al-8Cu-2Re-Mn-La-Ce after adding Al-La-Ce intermediate alloy. Among them, Fig.8 (a) and 8 (b) are the metallographic structure distribution of Al-8Cu-2Re-Mn (sample 2) before and after the surface corrosion, and Fig. 8 (c) and 8 (d) are the metallographic structure distribution of Al-8Cu-2Re-Mn-La-Ce (sample 6) before and after the surface corrosion.



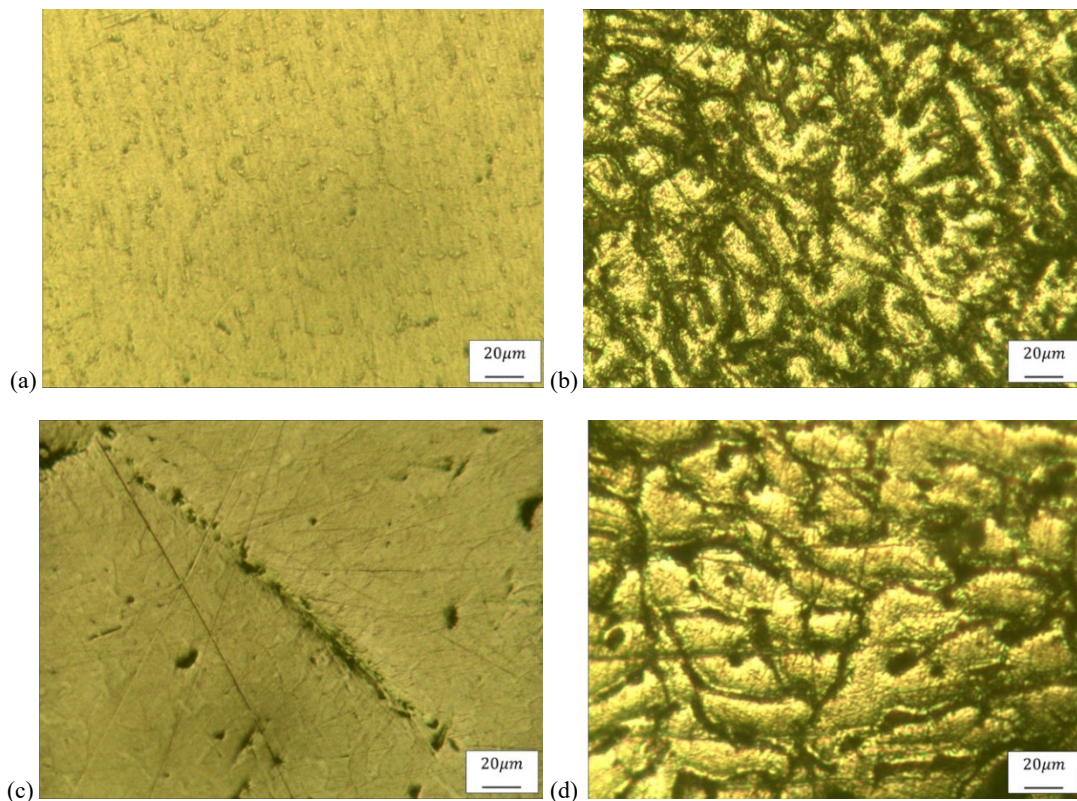


Fig. 8. Metallography of samples before and after corrosion (a) the metallographic structure of the corroded Al-8Cu-2Re-Mn alloy, (b) the microstructure diagram of the corroded Al-8Cu-2Re-Mn alloy, (c) the microstructure diagram of the uncorroded Al-8Cu-2Re-Mn-La-Ce alloy, (d) the microstructure diagram of the corroded Al-8Cu-2Re-Mn-La-Ce alloy

It can be observed from Fig. 8 (a) that before corrosion, black clumps with different sizes and density distributions are scattered out on the surface of the aluminum matrix, showing chaos on the whole. With a high probability, the phases such as  $\text{Al}_2\text{Cu}$ ,  $\text{Al}_6\text{Mn}$ , and  $\text{Al}_3\text{Re}$  precipitated randomly and distributed uniformly on the surface of the aluminum matrix without apparent aggregation phenomenon [42, 43]. However, it can be observed from Fig. 8 (c) that after the addition of mixed RE aluminum alloy surface along the grain boundary, there are apparent long needle-long strip enrichment structures. The structure has a green color and strong contrast with the aluminum matrix, and the surface is smooth and uniform. In addition, the surrounding small point-like block structures are clustered, and there is an apparent second-phase concentration.

H.c.Liao et al. [43] had confirmed that rare earth elements would preferentially precipitate along the grain boundary edge, and various second phases containing rare earth would also precipitate along the rare earth-rich area. It means that the addition of rare earth elements dramatically affects the process of grain boundary and second-phase formation in aluminum alloy. The growth distribution of this second phase also has a significant impact on the various properties of the material. The aggregation of the second phase strengthens the bonding tightness of the interface and enhances the strength and hardness of the material to a certain extent.

By comparing Fig. 8 (b) and Fig. 8 (d), it can be observed that the addition of mixed RE on the corrosion performance of the material. Fig. 8 (b) shows that the surface of the aluminum matrix generally produces black shadows and shallow corrosion structures, and the corrosion path spreads along the grain boundaries to a certain extent. The depth of corrosion per unit area is not significant, but the coverage area of the corrosion area is vast.

In Fig. 8 (d), the corrosion situation has changed significantly. It can be observed that there are apparent skeletal corrosion veins in the metallographic diagram, and the corrosion degree in the veins is more profound than that in Fig. 8 (b). Meanwhile, the surface of the aluminum matrix around the veins remains bright. It is shown that the aluminum matrix is protected preferentially in the corrosive environment. Combined with the observation results in Fig. 8 (c) and Fig. 8 (d), it is reasonable to believe that the priority corrosion is the second phase, such as  $\text{Al}_8\text{Cu}_4\text{Ce}$ ,  $\text{Al}_3\text{CuCe}$ , and  $\text{Al}_6\text{Cu}_6\text{La}$  in the rare earth enrichment region [44-46]. To a certain extent, this shows that in a corrosive environment, the second phase containing rare earth is preferentially corroded as the anode. At the same time, the aluminum matrix is protected as the cathode. The addition of mixed RE indirectly enhances the corrosion resistance of the material.

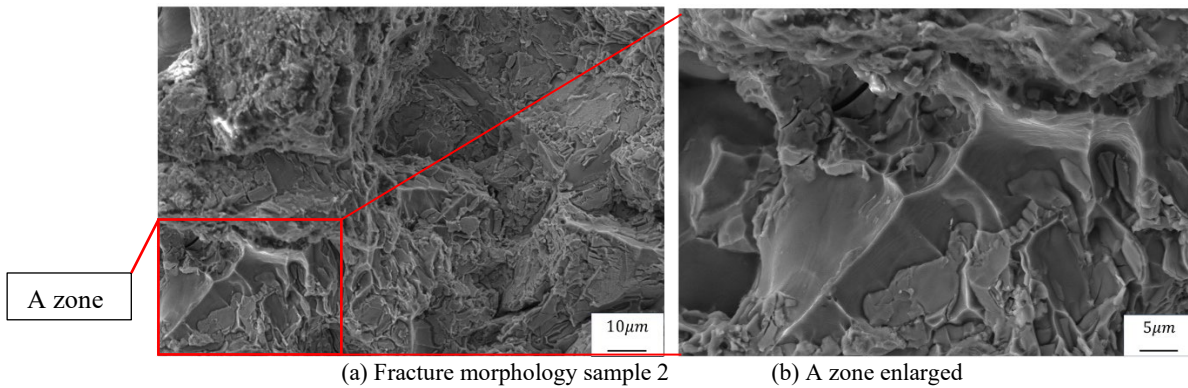
### 3.2.2. Fracture structure

In order to compare the reinforcement effect of mixed rare earth elements (La, Ce) on the alloy material, the fracture morphology of

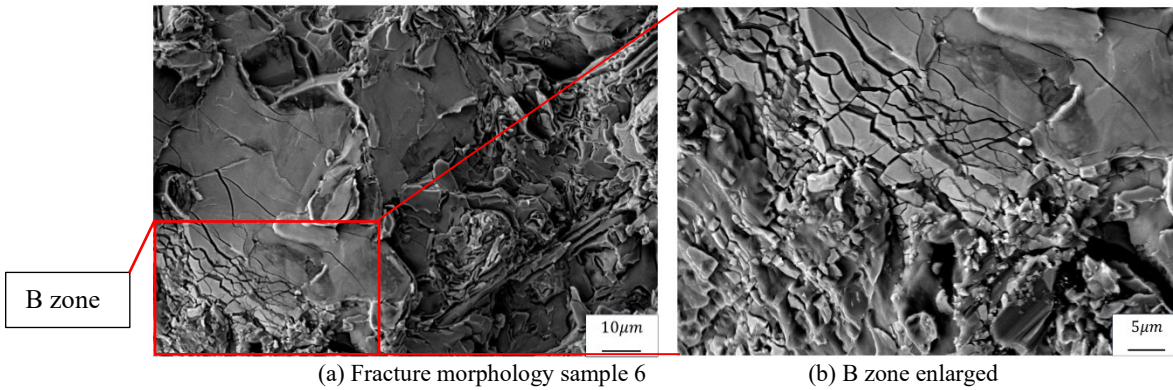


the samples with the best strength and hardness (sample 2 and sample 6) of the alloy material after tension was photographed and

analyzed. The characterization results are shown in Fig. 9 and Fig. 10.



(a) Fracture morphology sample 2 (b) A zone enlarged  
Fig. 9. SEM of fracture morphology of sample 2



(a) Fracture morphology sample 6 (b) B zone enlarged  
Fig. 10. SEM of fracture morphology of sample 6

Fig. 9 shows the fracture morphology of sample 2. The fracture morphology of sample 2 shows a scarp structure with uniform and dense fracture, and the scarp is attached to a flat platform structure. It can be seen that the platform grows along the scarp and preferentially fractures the scarp, leaving a large number of tearing rib structures. The angle of these tearing edges is sharp, and the cliffs in small areas are steep. This fracture surface makes the crack path more complicated, improves the strength of local areas, and limits the expansion of cracks, which is conducive to enhancing the material's ductility and improving the strength and hardness of the material.

After adding Al-La-Ce intermediate alloy, the fracture morphology of the sample changes obviously. As shown in Fig. 10, the fracture of sample 6 shows a lot of cross-sectional platform structures. This kind of structure has a significant impact on the internal anisotropy of the material. This kind of platform structure is very resistant to the load perpendicular to the platform direction. Just like it is easier to snap a pencil from the side than pull a broken pencil from the front. At the same time, from the enlarged Fig. 10 (b), it can be observed that the width of the material crack gradually expands from the middle of the platform to the periphery. It shows that the resistance of the structure to transverse load is weak, and the addition of rare earth materials reduces the transverse strength

and shear resistance of the material and negatively affects the plasticity of the material.

### 3.3. Analysis of calculation results

#### 3.3.1. Work function and adsorption energy

Classify and summarize the data on the electronic work function and surface adsorption energy calculated in this study. Two tables were prepared based on different cutoff surfaces and adsorption points. Tables 6 and 7 show the calculation results of adsorption energy and work function for different adsorbents of mixed RE adsorbed on  $Al_2Cu$  (001) surfaces with different cutoff surfaces. The difference  $\Delta W$  between the work functions calculated in Tables 6 and 7 is calculated based on  $W_{Al-Al_2Cu} = 4.12$  and  $W_{Cu-Al_2Cu} = 4.23$ , respectively. The results show that the adsorption energy generated by the 18 adsorption modes of mixed rare earth elements (La, Ce) on the surface of  $Al_2Cu$  (001) ranges from -1.43 to -4.47 eV. All of these are lower than the physicochemical critical adsorption energy (-0.415 eV) [32], indicating that multiple adsorption modes of mixed rare earth elements on the surface of  $Al_2Cu$  (001) can generate stable chemical adsorption.

Table 6.

Work functions and adsorption energies of various adsorption modes on the Al cutoff surface

| Adsorption | Position | Fermi level $E_F$ (eV) | Vacuum level $E_{vac}$ (eV) | Work function $E_{x/as}$ (eV) | Work function difference $\Delta W$ (eV) | Adsorption energy $E_{ad}$ (eV) | Terminal atom |
|------------|----------|------------------------|-----------------------------|-------------------------------|--|---------------------------------|---------------|
| La-Ce      | B        | 3.85                   | 7.62                        | 3.77                          | -0.36                                    | -2.36                           | Al-Ce-La      |
|            | V        | 3.76                   | 6.98                        | 3.22                          | -0.9                                     | -2.59                           | Al-Ce-La      |
|            | T        | 1.93                   | 4.66                        | 2.73                          | -1.39                                    | -2.11                           | Al-Ce-La      |
| Ce         | B        | 2.98                   | 6.56                        | 3.58                          | -0.54                                    | -2.34                           | Al-Ce         |
|            | V        | 2.97                   | 6.30                        | 3.33                          | -0.80                                    | -2.91                           | Al-Ce         |
|            | T        | 2.78                   | 6.53                        | 3.75                          | -0.37                                    | -2.31                           | Al-Ce         |
| La         | B        | 4.83                   | 7.31                        | 2.48                          | -1.64                                    | -2.26                           | Al-La         |
|            | V        | 2.46                   | 6.08                        | 3.62                          | -0.5                                     | -2.81                           | Al-La         |
|            | T        | 5.14                   | 7.58                        | 2.44                          | -1.68                                    | -2.22                           | Al-La         |

Table 7.

Work functions and adsorption energies of various adsorption modes on the Cu cutoff surface

| Adsorption | Position | Fermi level $E_F$ (eV) | Vacuum level $E_{vac}$ (eV) | Work function $E_{x/as}$ (eV) | Work function difference $\Delta W$ (eV) | Adsorption energy $E_{ad}$ (eV) | Terminal atom |
|------------|----------|------------------------|-----------------------------|-------------------------------|--|---------------------------------|---------------|
| La-Ce      | B        | 4.11                   | 7.21                        | 3.10                          | -1.13                                    | -2.46                           | Cu-Ce-La      |
|            | V        | 4.33                   | 6.76                        | 2.43                          | -1.79                                    | -4.23                           | Cu-Ce-La      |
|            | T        | 3.99                   | 6.72                        | 2.73                          | -1.50                                    | -2.05                           | Cu-Ce-La      |
| Ce         | B        | 2.02                   | 4.52                        | 2.50                          | -1.73                                    | -2.61                           | Cu-Ce         |
|            | V        | 3.24                   | 6.18                        | 2.94                          | -1.29                                    | -4.47                           | Cu-Ce         |
|            | T        | 3.02                   | 5.66                        | 2.64                          | -1.59                                    | -1.66                           | Cu-Ce         |
| La         | B        | 3.26                   | 6.66                        | 3.4                           | -0.83                                    | -2.85                           | Cu-La         |
|            | V        | 3.8                    | 6.66                        | 2.86                          | -1.37                                    | -4.21                           | Cu-La         |
|            | T        | 3.01                   | 6.45                        | 3.44                          | -0.79                                    | -1.43                           | Cu-La         |

The following biaxial columnar plot can be used to visually observe the comparison of different adsorption modes on the two cutoff surfaces based on the calculated data in the above Tables 6 and 7. And Fig. 11 and Fig. 12 show the work function difference and adsorption energy data of each adsorption mode on the Al and Cu cutoff surfaces, respectively. The line chart represents the distribution of adsorption energy of the material  $E_{ad}$  (eV), the bar chart represents the distribution of work function difference  $\Delta W$  (eV), and the X-axis coordinates represent different adsorption

points. For example, among the three brown cylinders in Fig. 11, the brown cylinder in the middle of the figure is the highest. This means that the work function difference  $\Delta W$  (eV) is the largest when the Ce element is adsorbed alone at the V position. Because the values of work function and adsorption energy are negative, which is inconsistent with the trend of conventional coordinate axes, so the absolute values of the two series of data of the Y axis of Fig. 11 and Fig. 12 is used.

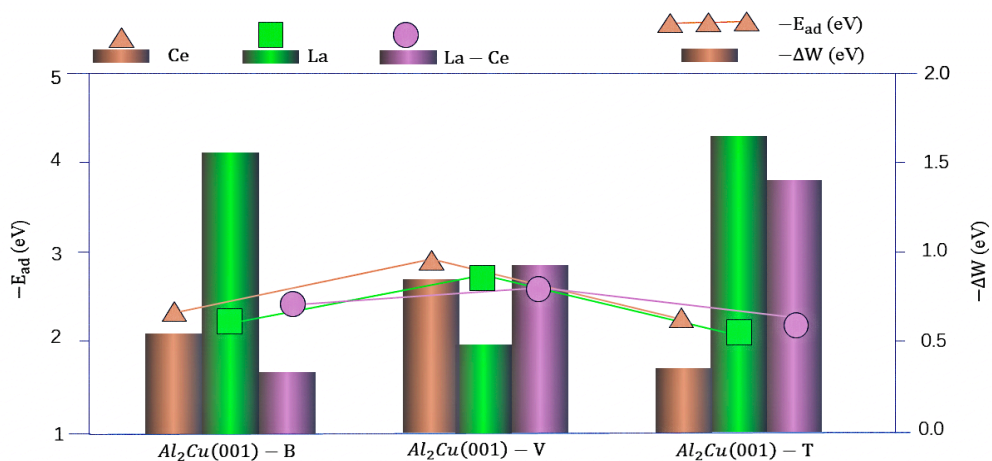


Fig. 11. Work function and adsorption energy of each adsorption mode on Al cutoff surface

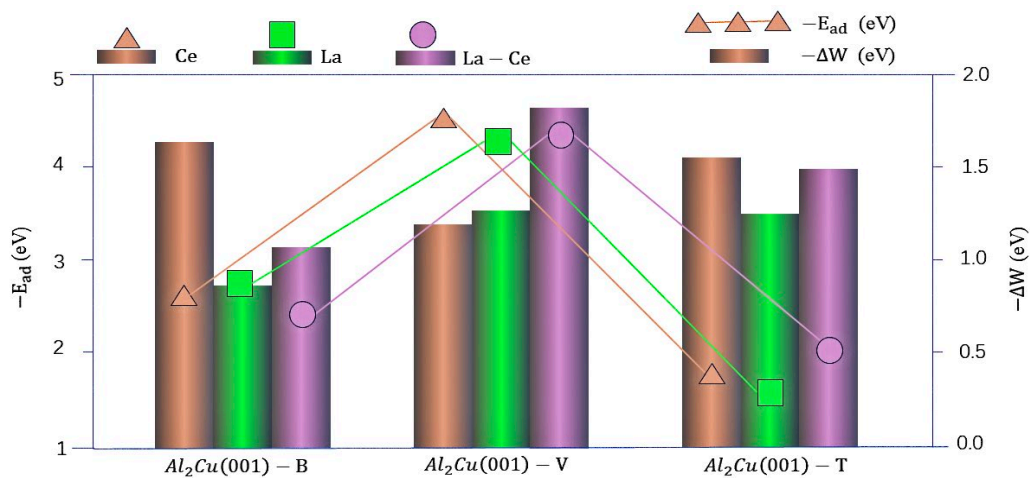


Fig. 12. Work function and adsorption energy of each adsorption mode of Cu cutoff surface

It can be seen from Fig. 11 and Fig.12 that compared with other highly symmetric sites, vacancy (V) exhibits relatively large adsorption energy on different adsorption quality models of the two cutoff surfaces, among which vacancy (V) on the Cu- $Al_2Cu$  (001) surface exhibits the largest adsorption energy and the most stable adsorption results. The adsorption energies of La, Ce and La-Ce molecule are  $V-E_{ad-La} = -4.21$  eV,  $V-E_{ad-Ce} = -4.47$  eV,  $V-E_{ad-La-Ce} = -4.23$  eV, respectively. The above three models with high stability will be used to calculate the band structure, state density, and elastic constant in the next step.

It can also be observed that the adsorption energy of each adsorption mode on the cutoff surface of Cu- $Al_2Cu$  (001) is smaller than that of the transverse comparison object on the Cutoff surface of Al- $Al_2Cu$  (001). It shows that the mixed RE is more stable at the Cu cutoff surface when  $Al_2Cu$  (001) is adsorbed on the surface. This also indicates that the mixed rare earths (La, Ce) will preferentially bond with Cu atoms in the reaction.

It is observed in Fig. 12 that when each adsorbent is adsorbed on the top of the cutoff surface of copper, the adsorption energy results are inconsistent with the above conclusions. This is because the model of Cu- $Al_2Cu$  (001) cutoff surface presents a structural symmetry problem at top position (T). Because the adsorbent of mixed RE has a larger atomic radius than that of Cu atom, the adsorbent is located at the edge of the crystal cell at the top position, and the boundary of the crystal cell escapes a lot of electron energy

from La and Ce atoms, resulting in a phenomenon of low adsorption energy.

From the numerical point of view, the overall work function of  $Al_2Cu$  after adsorption presents a sizeable downward trend. The work function difference  $\Delta W$  (eV) of the Al cutoff surface ranges from -0.36 to -1.68 eV, and the transversely compared work function difference  $\Delta W$  (eV) of the Cu cutoff surface ranges from -0.79 to -1.79 eV. The difference in the minimum peak value shows that the Cu cutoff surface reduces the work function more obviously. From the bar chart of work function difference in Fig. 11 and Fig. 12, it is also evident that the work function difference  $\Delta W$  (eV) on the Cu cutoff surface is also more larger on the whole, indicating that the adsorption behavior of mixed RE on the  $Al_2Cu$  (001) crystal surface has a more prominent effect on reducing the work function when it occurs on the Cu cutoff surface.

### 3.3.2. Energy band and density of states

In order to better understand the electronic structure and characteristics of the Al/Cu- $Al_2Cu$  (001) surface system adsorbed by mixed rare earth (La Ce), the energy band and density of electronic states (DOS) before and after adsorption on the surface of Cu- $Al_2Cu$  (001) were calculated, as shown in Fig. 13. Fig. 13 (a) shows the state energy band and state density before Cu- $Al_2Cu$  (001) adsorption; Fig. 13 (b), Fig. 13 (c), and Fig. 13 (d) show the state energy band and state density of La-Ce co-adsorption, Ce single adsorption, and La single adsorption.

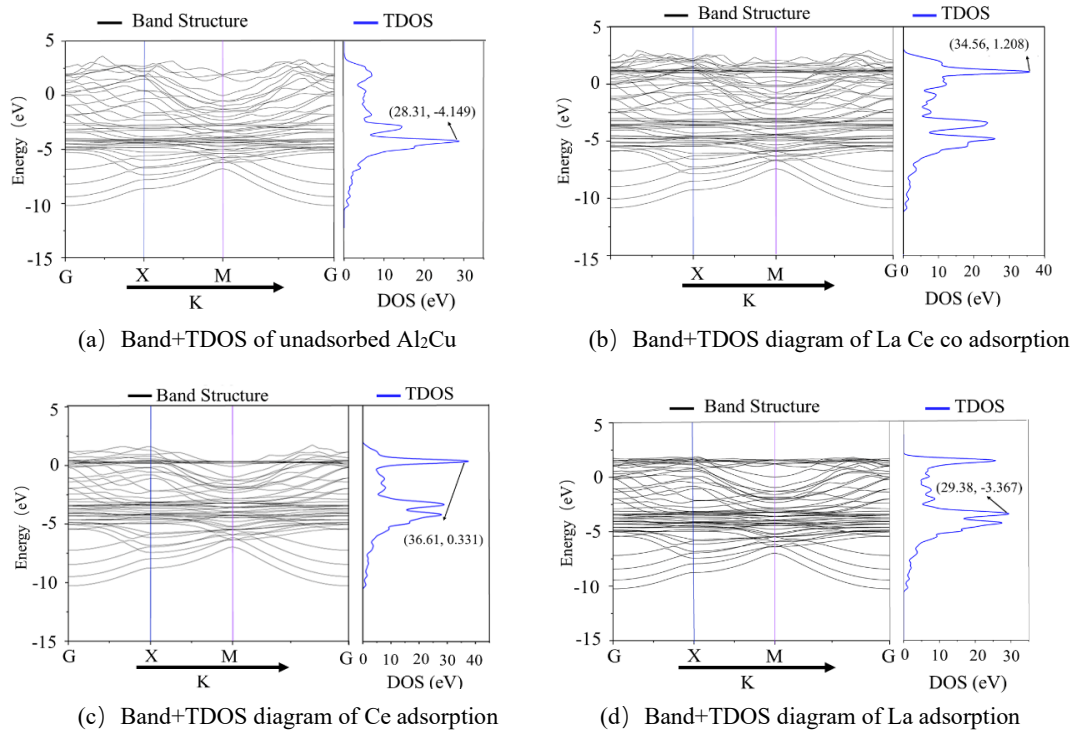


Fig. 13. Band+TDOS diagrams for various adsorption modes

Firstly, both before and after adsorption, the conduction band intersects with the Fermi level, and the atomic state density of the whole system at the Fermi surface is not 0. Electrons in the conduction band can move freely, and conduction current is formed by the valence band passing through the Fermi level into the conduction band. This phenomenon indicates that the conductivity of  $\text{Al}_2\text{Cu}$  is not affected by the addition of rare earth. Because electrons in orbits far away from the Fermi surface do not participate in bonding, the effect on the electronic structure and material properties is small, so only the electronic structure of Fermi-level attachments is discussed in this study.

The comparison of the band structure before and after adsorption shows that the conduction band density of the system increases significantly after adsorption, and the high energy part of the conduction band is mainly provided by the adsorbent atoms (La, Ce). Through the previous research results on the electron localization of the outer layers of rare earth elements, we can even know that the dense electrons in the conduction band come from the outer d and f orbitals of adsorbate atoms (La, Ce) [47]. This results in a narrow bandwidth of the conduction band and a shift towards the Fermi level, with robust electron localization and a relatively large effective mass in the conduction band.

Secondly, the total density of states (TDOS) shows the specific composition of electronic states in the band structure, and the minimum peak of valence band energy in each adsorption mode appears steadily at  $-10.1\text{eV}$ . The densest peaks of the energy state

appear near  $-4.15\text{eV}$  in the non-adsorption state, and new peaks appear above the Fermi level after adsorption. They are  $1.22\text{eV}$  when La-Ce is adsorbed together,  $0.33\text{eV}$  when Ce is adsorbed alone, and  $1.33\text{eV}$  when La is adsorbed alone. The pseudo-energy gap can also be found in the DOS diagram. That is, the DOS values between the left and right peaks at the Fermi level are not 0, which reflects the covalence of the bonding state of the alloy system [48].

### 3.3.3. Calculation of elastic constant

Table 8 shows the calculation results of the elastic constants of  $\text{Al}_2\text{Cu}$  in different adsorption states, according to which the mechanical properties of the materials in Table 9 can be calculated. It can be seen from the calculation results in Table 9. That  $\text{Al}_2\text{Cu}$  in the presence of the P4/mmm space group shows the characteristics of plastic material, which is consistent with the results of the tensile test of the test rod. The elastic constants of the surface model  $\text{Al}_2\text{Cu}(001)$  are calculated, and the results show that the bulk modulus, Young's modulus, and shear modulus are slightly reduced compared with the data of the original cell. It is concluded that the size gap between the a, b, and c axes in the surface model of  $\text{Al}_2\text{Cu}(001)$  is too large, and the upward response of all parties is not as balanced as that of the  $\text{Al}_2\text{Cu}$  cells when the stress-strain method is used to calculate the elastic constant. The influence of mixed rare earth adsorption on the elastic constant of the material was then calculated, and the numerical results of the  $\text{Al}_2\text{Cu}(001)$  surface were used as the reference.

Table 8.

Calculation results of elastic constants of each model

| Computational Object     | $C_{11}$ (GPa) | $C_{12}$ (GPa) | $C_{13}$ (GPa) | $C_{33}$ (GPa) | $C_{44}$ (GPa) | $C_{66}$ (GPa) |
|--------------------------|----------------|----------------|----------------|----------------|----------------|----------------|
| References [37]          | 185.0          | 12.0           | 68.0           | 142.0          | 51             | 38             |
| Al <sub>2</sub> Cu       | 189.5          | 12.2           | 70.0           | 136.4          | 58.7           | 53.3           |
| Al <sub>2</sub> Cu (001) | 214.8          | 5.73           | 36.8           | 119.9          | 42.2           | 30             |
| Ce                       | 233.1          | 23.7           | 37.6           | 112.8          | 50.0           | 59.7           |
| La                       | 242.7          | 19.6           | 41.3           | 140.1          | 42.3           | 60.2           |
| La-Ce                    | 227.3          | 26.7           | 40.4           | 83.0           | 70.7           | 74.3           |

Table 9.

Calculated mechanical properties of each model

| Computational Object     | $B$ (GPa) | $E$ (GPa) | $G$ (GPa) | $\nu$ | $B/G$ | $H_V$ (GPa) | $u_M$ |
|--------------------------|-----------|-----------|-----------|-------|-------|-------------|-------|
| Al <sub>2</sub> Cu       | 91.3      | 138.9     | 55.8      | 0.246 | 1.64  | 8.78        | 1.55  |
| Al <sub>2</sub> Cu (001) | 77.3      | 123.1     | 49.8      | 0.235 | 1.55  | 8.78        | 1.80  |
| Ce                       | 82.5      | 146.9     | 61.0      | 0.203 | 1.35  | 12.4        | 1.64  |
| La                       | 90.3      | 147.1     | 59.9      | 0.228 | 1.51  | 10.4        | 2.13  |
| La-Ce                    | 76.3      | 155.9     | 67.2      | 0.159 | 1.13  | 17.0        | 1.08  |

The calculated values of Vickers hardness  $H_V$  and machining index  $u_M$  before and after adsorption of Al<sub>2</sub>Cu primitive cell and mixed rare earth in Table 9 above are shown in Fig. 14, where the blue bar chart represents the numerical distribution of calculated

Vickers hardness  $H_V$ , corresponding to the Y-axis unit on the left. The yellow bar chart represents the calculated machining index  $u_M$ , corresponding to the right Y axis.

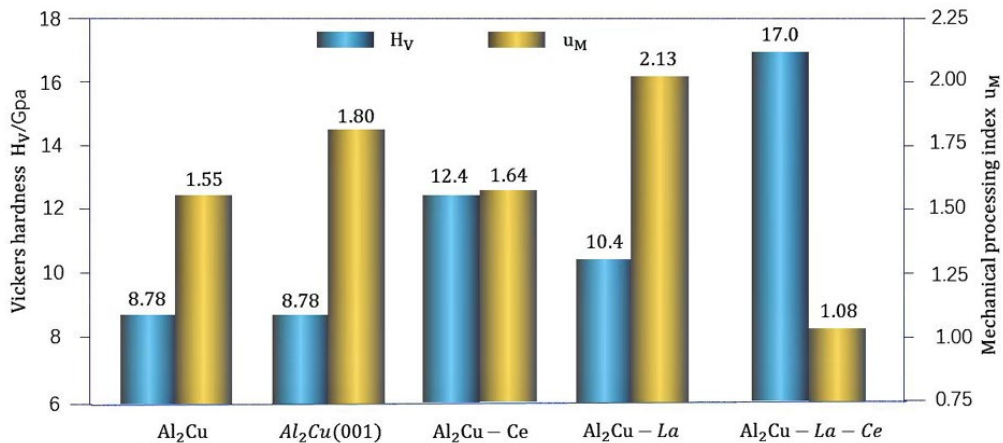


Fig. 14. Vickers hardness  $H_V$  and machining index  $u_M$  of pure surface adsorption models

A comprehensive analysis of the results of Table 9 and Fig. 14 shows that the bulk modulus, shear modulus, and Young's modulus of the material have a certain amount of increase after the adsorption of La element. The increases were  $\Delta B=13$  (GPa),  $\Delta G=10.1$  (GPa) and  $\Delta E=24$  (GPa). The results show that the compressive resistance, shear resistance, and stiffness of the material are enhanced. The calculated results of  $B/G$  and  $\nu$  after La adsorption of Al<sub>2</sub>Cu (001) alone have little difference from the results of the comparison basis. Moreover, the machining performance is improved from  $H_V=8.78$  to  $H_V=10.4$  compared to before adsorption. In addition, the machining index has improved significantly ( $u_M$  increased from 2.13). This series of results shows that under the influence of La element alone, the mechanical properties of the material are improved, and the machinability of

the material is enhanced under the premise of maintaining the plasticity of the material.

The results show that the elastic modulus of the adsorbed material increases by  $\Delta B=5.2$  (GPa),  $\Delta G=11.2$  (GPa) and  $\Delta E=23.8$  (GPa), respectively. According to the calculation results of the hardness  $H_V$  of the material, the hardness  $H_V$  of the material increases to 12.4 (GPa) after the adsorption of Ce, which is 41% higher than that without the addition of rare earths. However, the adsorption of Ce also reduced the Poisson's ratio  $\nu$  by 13.6% to 0.203, and the calculated  $u_M$  value was also reduced. This shows that the elastic modulus and hardness (mechanical strength properties) of the material are significantly increased after the adsorption of Ce, but the machinability coefficient of the material is reduced.



Last but not least, when La-Ce adsorbs  $\text{Al}_2\text{Cu}$  (001) in the compound state, the interaction between La and Ce elements is pronounced. From the change of elastic constant, Young's modulus and shear modulus are extremely increased under the condition that the bulk modulus is basically unchanged, and the increases are  $\Delta G=17.4$  (GPa) and  $\Delta E=32.8$  (GPa) respectively. The Vickers hardness was strengthened to  $H_V=17$  (GPa), an extremely high increase, but this adsorption mode caused the Poisson ratio  $\nu$  of the material to drop sharply to 0.159, and the machining index  $UM$  fell sharply to 1.08. The results show that La-Ce molecule adsorption of  $\text{Al}_2\text{Cu}$  can extremely increase the strength and hardness of the material, and extremely reduce the plasticity of the material.

## 4. Mechanism analysis

### 4.1 Strengthening mechanism of mechanical properties

Fig. 15 shows the microstructure, energy spectrum distribution of elements, and analysis results of elements content of test rod 6, Al-8Cu-2Re-Mn-La-Ce, with rare earth elements added, under an electron microscope. Fig. 15 (a) is the microstructure of test rod 6, Fig. 15 (b) shows the distribution of elements of test rod 6. Fig. 15 (c) is the total energy spectrum of this surface of Fig. 15 (a), as well as the percentage of element mass (wt%) and the percentage of atom number (at%).

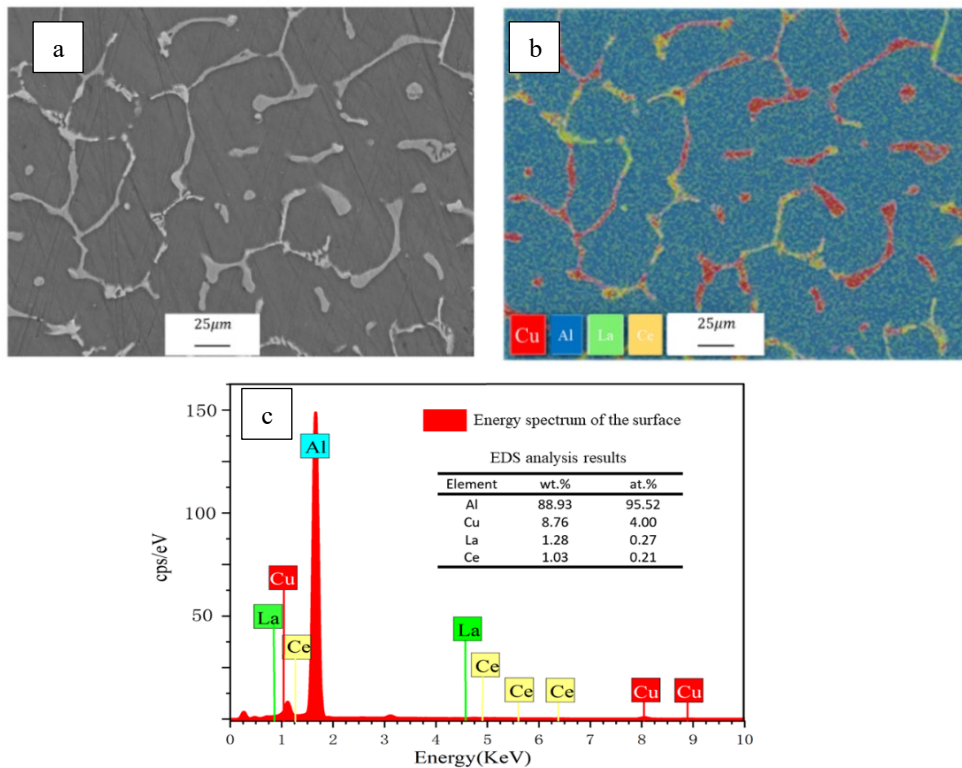


Fig. 15. SEM microstructure and EDS analysis of Al-8Cu-2Re-Mn-La-Ce alloy

In Fig. 15 (a), it can be observed that the second phase forms a grid-like boundary, which makes the radius of the lattice smaller. The distribution of this surface element can be observed in Fig. 15 (b), where the Cu element is the dominant component in the second phase. As shown in Fig. 15 (b) and Fig. 15 (c), the content of rare earth elements in the test rod is 1.28wt% of La and 1.03wt% of Ce, and the content of Cu element is 8.76wt.%, which is the same as the content designed by our experiment. In addition, it can be seen

from Fig. 15 (b) that rare earth elements are enriched in the region where Cu and Al form the second phase, indicating that rare earth elements prefer reacting with Cu elements in ZL206's second phase containing copper. This phenomenon coincides with the calculation result of adsorption energy in Chapter 3.3.1. The calculation results in Chapter 3.3.1 show that rare earth elements are more likely to bind to the Cu cutoff surface of  $\text{Al}_2\text{Cu}$  (001). That is, rare earth elements are more likely to react with Cu elements. This

phenomenon shows that rare earth will be enriched in the surrounding region of the second phase containing copper, such as  $\text{Al}_2\text{Cu}$ , after adding ZL206, forming a rare earth enrichment region.

Metallography observation found that the composite material with mixed RE had a prominent needle structure. According to the growth inhibition theory, the solubility of rare earth elements in Al alloys is limited, which usually preferred enrichment and precipitation in the solidification process and hindered the grain growth of  $\alpha$ -Al phase [49]. This is because the atomic radius of La and Ce is larger than that of Al and Cu, and the crystal structure difference is large, so the solid solubility of rare earth elements in aluminum alloys is small, and it is easier to enrich at the grain boundaries.

The crystal solidification process is shown in Fig. 16. During the crystallization process of the composite material, the  $\alpha$ -Al phase will be preferred out. At this time, a few rare earth elements dissolved in the  $\alpha$ -Al phase will spontaneously cause a certain matrix lattice distortion due to its large radius, resulting in an increase in energy and a decrease in system stability. Based on the principle of minimum energy, the rare earth atoms are enriched on the grain growth surface, and along grain boundaries to form the Rich RE (Rich rare earth region) in the Fig. 16, which accords with the characteristics of the needle structure observed in the metallographic experiment.

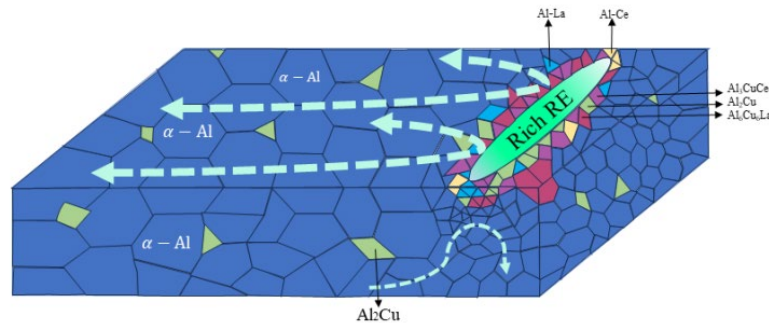


Fig. 16. Schematic diagram of precipitation in heterogeneous enrichment area

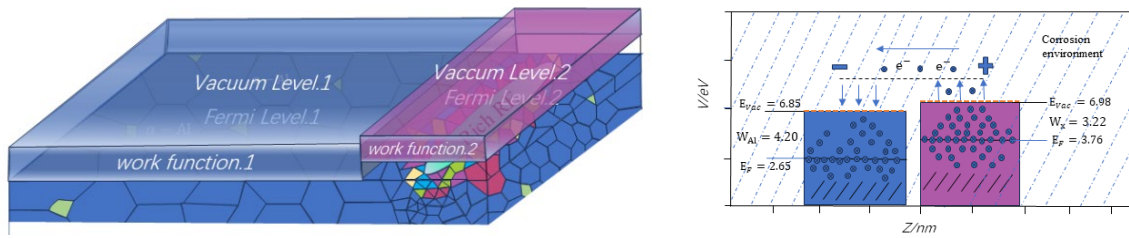
Literature studies [21-23] have shown that, due to the active chemical properties of rare earth elements, it is easy to react with metal elements. The adsorption simulation calculations of this study are also consistent with this conclusion. Therefore, it can be seen that the second phase structure modified by mixed rare earths (La, Ce) will be precipitated in the vicinity of the rare earth rich area, such as  $\text{Al}_3\text{Cu}_4\text{Ce}$ ,  $\text{Al}_3\text{CuCe}$ ,  $\text{Al}_6\text{Cu}_6\text{La}$ , and other heterogeneous structures, forming a heterogeneous structure rich area with tiny grains. The normal second phase in this region has not been modified by rare earths and also exhibits limited growth and small grain size due to space constraints.

This series of phenomena also leads to the growth of the  $\alpha$ -Al phase in this area of the annex being greatly hindered, the closer to the rare earth rich area, the smaller the space for  $\alpha$ -Al phase growth, the smaller the grain size, so as to play a fine grain effect. Moreover, because the calculation results proved that the strength of the second phase after rare earth modification was improved, a high strength strengthening zone was formed along the grain boundary inside the material after the addition of mixed rare earth, which improved the strength and hardness of the material. In addition, because there are many interfacial intervals between this region and the aluminum matrix region, and the plasticity of the regional organization itself is weak, based on this mechanism, the plasticity of the material is reduced to a certain extent.

## 4.2. Corrosion resistance mechanism

The influence mode of mixed RE on the electronic work function of  $\text{Al}_2\text{Cu}$  surface is explored by simulation calculation in chapter 3.3.1. The results show that the electronic work function of  $\text{Al}_2\text{Cu}$  can be reduced by rare earth elements. From the forming and solidification process of the above composite materials, we know that the second phase containing rare earth will be concentrated in the rare earth rich area after adding rare earth. Among them, the work function of Al-Cu-Re (Rare Earth), which is dominated by content, is less than that of Al matrix. The work function of mixed RE is also lower than that of Al matrix ( $W_{\text{La}}=3.5$  eV,  $W_{\text{Ce}}=2.9$  eV) [33].

The thickness of the semitransparent region in Fig. 17 (a) represents the work function of the material. There is a significant gradient between the work function of the rare earth rich region and the surrounding matrix. This phenomenon leads to a significant difference in the physical properties of the two regions. In the Fig. 17 (a), work function. 1 represents the work function of the  $\alpha$ -Al phase, and work function. 2 represents the overall work function of the rare earth rich area. (The work function of the rare earth rich area in the Fig. 17 (b) is taken as an example of a data point in the previous article  $W_{\text{A}}=3.22$  eV,  $E_{\text{Vac}}=6.98$  eV,  $E_{\text{F}}=3.76$  eV).



(a) Step distribution diagram of work function

(b) Schematic diagram of cathodic protection mechanism

Fig. 17. Schematic diagram of corrosion mechanism

Studies[50] have shown that in a chemical corrosion environment, if the work function of the inclusion or the second phase material in the material is lower than that of the aluminum matrix, they will be preferentially dissolved as the anode, while the aluminum alloy matrix acts as the cathode to be protected. As shown in Fig. 17 (b), the rare earth rich area is more likely to lose electrons and be preferentially corroded in a corrosive environment, while the Al matrix is protected. From the above calculation results, it can be seen that the addition of rare earth causes a general decline in the electronic work function of the rare earth rich area, indicating that the area as a whole will be preferentially corroded to protect the aluminum matrix. (Aluminum matrix work function reference value is  $W_{Al}=4.28$ , the experimental results calculated is  $W_{Al}=4.20$ ,  $E_{vac}=6.85$ ,  $E_F=-2.65$  [32].)

It is also known from the above calculation results that the Fermi level value of the material after adding rare earth has an upward trend compared with that before modification. At non-absolute zero, electrons spontaneously escape, and the Fermi level is the most electron dense level in the material at this time. A higher value of the Fermi level means that the highest energy potential of the electron filling increases, and the orbital energy of the outermost electron also increases, which also means that the material's surface is more likely to lose electrons.

A preliminary mechanism was obtained. The work function of the material was reduced by increasing the Fermi level inside the material by adding mixed RE. As a result, in the chemical corrosion environment, the modified second-phase material is more likely to lose electrons as the anode and be preferentially corroded. At the same time, the Al matrix is protected, which indirectly strengthens the corrosion resistance of the aluminum copper alloy material.

## 5. Conclusions

Casting experiments were conducted to study the casting aluminum-copper alloy ZL206, and the properties of the alloy were analyzed after the addition of mixed RE, and the mechanism of strengthening aluminum-copper alloy with mixed rare earth was explored. To further explore its enhanced mechanism, the first principles method was used to model and calculate the work function, elastic properties, and electronic structure of mixed RE after adsorption in the second phase  $Al_2Cu$  (001). The following research conclusions were obtained.

(1) According to the experiment results, the strength and hardness of the composite material increased 10.2% and 6.2%

respectively after the addition of mixed RE, while the elongation and machinability coefficient of the material were affected.

(2) The simulation results show that rare earth elements La and Ce have active chemical properties and can stably adsorb on the surface of  $Al_2Cu$  and react with Al and Cu elements to form covalent bonds. The adsorption of rare earth elements generally reduces the work function of the second phase of  $Al_2Cu$ . Adding rare earth increases the Fermi level value of the second phase, which strengthens the strength and hardness of the second phase but sacrifices some toughness and machining properties.

(3) Two kinds of RE modification mechanisms were evaluated. First, because of the sizeable atomic radius of RE, the precipitation would be concentrated on the grain boundary surface according to the minimum energy theorem, which would make the grains be refined. Second, the second phase containing rare earth is also increased, which due to the RE adding could hinder the growth of the  $\alpha$ -Al phase. So the mechanical properties of the material are improved. And the work function and higher Fermi level value is low in this zone and the preferentially corroded in a chemical corrosion environment, and the aluminum matrix will be protected.

During this study, the microscopic structure and macroscopic properties are linked through atomic simulations. The strengthening mechanism of material properties was discussed with a new method, and the material properties were explained from different angles. However, the relationship between microstructures and macroscopic properties remains to be further explored.

## Acknowledgments

This research was financially supported by the Guizhou Industry Simulation Design & Innovation Center (QKZYD NO.[2016]4006). Moreover, this research was also financially supported by Doctoral Research Foundation of Guizhou Normal University (2017) and Guizhou Education Department Science and Technology research project serve for the "Four new" and "Four modernizations" (QJJ [2022] No. 005).

## References

- [1] Gan, L., Wen-ying, Q., Min, L., Le, C., Chuan, G., Xing-gang, L., Zhen, X., Xiao-gang, H., Da-quan, L., Hong-xing, L. & Qiang, Z. (2021). Semi-solid processing of aluminum and magnesium alloys: Status, opportunity, and challenge in

- China. *Transactions of Nonferrous Metals Society of China*. 31(11), 3255-3280. [https://doi.org/10.1016/S1003-6326\(21\)65729-1](https://doi.org/10.1016/S1003-6326(21)65729-1).
- [2] Wang, J. & Li, F. (2023). Research Status and prospective properties of the Al-Zn-Mg-Cu series aluminum alloys. *Metals*. 13(8), 1329, 1-24. <https://doi.org/10.3390/met13081329>.
- [3] Medvedev, A.E., Murashkin, M.Y., Enikeev, N.A., Valiev, R.Z., Hodgson, P.D. & Lapovok, R. (2018). Enhancement of mechanical and electrical properties of Al-RE alloys by optimizing rare-earth concentration and thermo-mechanical treatment. *Journal of Alloys and Compounds*. 745, 696-704. <https://doi.org/10.1016/j.jallcom.2018.02.247>.
- [4] Demétrio, K. B., Nogueira, A. P. G., Menapace, C., Bendo, T., & Molinari, A. (2021). Effect of nanostructure on phase transformations during heat treatment of 2024 aluminum alloy. *Journal of Materials Research and Technology*. 14, 1800-1808. <https://doi.org/10.1016/j.jmrt.2021.07.044>.
- [5] Hong, J., Linfan, Z., Biwei, Z., Ming, S. & Meifeng, H. (2022). Microstructure and mechanical properties of ZL205A aluminum alloy produced by squeeze casting after heat treatment. *Metals*. 12(12), 2037, 1-12. <https://doi.org/10.3390/met12122037>.
- [6] Krishna, N.N., Sivaprasad, K. & Susila, P. (2014). Strengthening contributions in ultra-high strength cryorolled Al-4% Cu-3% TiB<sub>2</sub> in situ composite. *Transactions of Nonferrous Metals Society of China*. 24(3), 641-647. [https://doi.org/10.1016/S1003-6326\(14\)63106-X](https://doi.org/10.1016/S1003-6326(14)63106-X).
- [7] Liu, F., Su, H., Liang, Y. & Xu, J. (2023). Fatigue performance on 7050 aluminum alloy by using ultrasonic vibration-assisted hole expansion strengthening. *The International Journal of Advanced Manufacturing Technology*. 128, 5153-5165. <https://doi.org/10.1007/s00170-023-12234-y>.
- [8] Harvey, (2013). Cerium-based conversion coatings on aluminium alloys: a process review. *Corrosion Engineering, Science and Technology*. 48(4), 248-269. <https://doi.org/10.1179/1743278213Y.0000000089>.
- [9] Martínez-Campos, A. Y., Pérez-Bustamante, F., Pérez-Bustamante, R., Rosales-Sosa, G., del carmen Gallegos-Melgar, A., Martínez-Sánchez, R., Carreño-Gallardo, C. & Mendoza-Duarte, J. M. (2021). Hot extrusion of an aerospace-grade aluminum alloy modified with rare earths. *Microscopy and Microanalysis*. 27(S1), 3396-3397. <https://doi.org/10.1017/S1431927621011673>.
- [10] Ding, W., Zhao, X., Chen, T., Zhang, H., Liu, X., Cheng, Y. & Lei, D. (2020). Effect of rare earth Y and Al-Ti-B master alloy on the microstructure and mechanical properties of 6063 aluminum alloy. *Journal of Alloys and Compounds*. 830, 154685, 1-11. (prepublish). <https://doi.org/10.1016/j.jallcom.2020.154685>.
- [11] Brachetti-Sibaja, S. B., Domínguez-Crespo, M. A., Torres-Huerta, A. M., Onofre-Bustamante, E., & La Cruz-Hernández, D. (2014). Rare earth conversion coatings grown on AA6061 aluminum alloys. Corrosion studies. *Journal of the Mexican Chemical Society*. 58(4), 248-269. <https://doi.org/10.29356/jmcs.v58i4.48>.
- [12] Ouyang, Y., Zhang, B., Jin, Z. & Liao, S. (1996). The formation enthalpies of rare earth-aluminum alloys and intermetallic compounds. *International Journal of Materials Research*. 87(10), 802-805. <https://doi.org/10.1515/ijmr-1996-871011>.
- [13] Xie, S.-K., Yi, R.X., Gao, Z., Xia, X., Hu, C.G. & Guo, X.Y. (2010). Effect of rare earth Ce on casting properties of Al-4.5 Cu alloy. *Advanced Materials Research*. 136, 1-4. <https://doi.org/10.4028/www.scientific.net/AMR.136.1>.
- [14] Xie, S.-K., Ai, Y.P., Xia, X., Yi, R.X., Gao, Z. & Guo, X.Y. (2011). Effects of Ce addition on the mobility and hot tearing tendency of Al-4.5 Cu alloy. *Advanced Materials Research*. 146, 481-484. <https://doi.org/10.4028/www.scientific.net/AMR.146-147.481>.
- [15] Knipling, K.E., Dunand, D.C. & Seidman, D.N. (2022). Criteria for developing castable, creep-resistant aluminum-based alloys—A review. *International Journal of Materials Research*. 97(3), 246-265. <https://doi.org/10.1515/ijmr-2006-0042>.
- [16] Belov, N.A., Naumova, E.A. & Eskin, D.G. (1999). Casting alloys of the Al-Ce-Ni system: microstructural approach to alloy design. *Materials Science and Engineering: A*. 271(1-2), 134-142. [https://doi.org/10.1016/S0921-5093\(99\)00343-3](https://doi.org/10.1016/S0921-5093(99)00343-3).
- [17] Hishiki, F., Akiyama, T., Kawamura, T., & Ito, T. (2022). Structures and stability of GaN/Ga<sub>2</sub>O<sub>3</sub> interfaces: a first-principles study. *Japanese Journal of Applied Physics*. 61(6), 065501. <https://doi.org/10.35848/1347-4065/ac5e90>.
- [18] Chen, S., Wang, Q., Liu, X., Tao, J., Wang, J., Wang, M. & Wang, H. (2020). First-principles studies of intrinsic stacking fault energies and elastic properties of Al-based alloys. *Materials Today Communications*. 24, 101085, 1-9. (prepublish). <https://doi.org/10.1016/j.mtcomm.2020.101085>.
- [19] Yan, C.W., Bo, L.Y., Peng, Z. & Bo, G.C. (2018). First principle study of electronic structures and optical properties of Ce-doped SiO<sub>2</sub>. *AIP Advances*. 8(5), 055125. <https://doi.org/10.1063/1.5024592>.
- [20] Yue, F., Jiaojiao, C., Chi, L., Tao, W., Hongchen, L. & Tao, S. (2021). A first-principle study on photoelectric characteristics of Ce-doped ZnO. *Ferroelectrics*. 573(1), 214-223. <https://doi.org/10.1080/00150193.2021.1890478>.
- [21] Ali, M.L. & Rahaman, M.Z. (2018). Investigation of different physical aspects such as structural, mechanical, optical properties and Debye temperature of Fe<sub>2</sub>ScM (M=P and As) semiconductors: A DFT-based first principles study. *International Journal of Modern Physics B*. 32(10), 1850121. <https://doi.org/10.1142/S0217979218501217>.
- [22] Wutthigrai, S., Ittipon, F., Sukit, L. & Kanoknan, P. (2022). A first principles investigation on the structural, elastic, and mechanical properties of MAX phase M<sub>3</sub>AlC<sub>2</sub> (M= Ta, Ti, V) as a function of pressure. *Computational Condensed Matter*. 30, e00638, 1-9. (prepublish). <https://doi.org/10.1016/j.cocom.2021.e00638>.
- [23] Zhang, J., Huang, Y., Mao, C. & Peng, P. (2012). Structural, elastic and electronic properties of  $\theta$  (Al<sub>2</sub>Cu) and S (Al<sub>2</sub>CuMg) strengthening precipitates in Al-Cu-Mg series alloys: first-principles calculations. *Solid State Communications*. 152(23), 2100-2104. <https://doi.org/10.1016/j.ssc.2012.09.003>.
- [24] Cornette, P., Costa, D. & Marcus, P. (2020). Relation between surface composition and electronic properties of native oxide films on an aluminium-copper alloy studied by DFT. *Journal*

- of the *Electrochemical Society*. 167(16), 161501. <https://doi.org/10.1149/1945-7111/abc9a1>.
- [25] China Aviation Industry Group. HB 962-2001 Casting Aluminum alloys[S]. Beijing: China National Defense Science, Technology and Industry Commission.2001.11.15.
- [26] China Iron and Steel Research Institute, GB/T 228-2002 Metallic materials-Tensile testing at ambient temperature[S]. Beijing: General Administration of Quality Supervision, Inspection and Quarantine of China, 2002.
- [27] Wang, S. & Fan, C. (2019). Crystal structures of Al<sub>2</sub>Cu revisited: understanding existing phases and exploring other potential phases. *Metals*. 9(10), 1037, 1-10. <https://doi.org/10.3390/met9101037>.
- [28] Mishnaevsky Jr, L. (2015). Nanostructured interfaces for enhancing mechanical properties of composites: Computational micromechanical studies. *Composites Part B: Engineering*. 68, 75-84. <https://doi.org/10.1016/j.compositesb.2014.08.029>.
- [29] Li, Y., Zhang, Z., Vogt, R., Schoenung, J. & Lavernia, E. (2011). Boundaries and interfaces in ultrafine grain composites. *Acta materialia*. 59(19), 7206-7218. <https://doi.org/10.1016/j.actamat.2011.08.005>.
- [30] Liu, Y., Xu, M., Xiao, L., Chen, X., Hu, Z., Gao, B., Liang, N., Zhu, Y., Cao, Y. & Zhou, H. (2023). Dislocation array reflection enhances strain hardening of a dual-phase heterostructured high-entropy alloy. *Materials Research Letters*. 11(8) 638-647. <https://doi.org/10.1080/21663831.2023.2208166>.
- [31] Maldonado, F. & Stashans, A. (2017). DFT study of Ag and La codoped BaTiO<sub>3</sub>. *Journal of Physics and Chemistry of Solids*. 102, 136-141. <https://doi.org/10.1016/j.jpics.2016.11.016>.
- [32] Loschen, C., Carrasco, J., Neyman, K.M. & Illas, F. (2007). First-principles LDA+ U and GGA+ U study of cerium oxides: Dependence on the effective U parameter. *Physical Review B*. 75(3), 035115. <https://doi.org/10.1103/PhysRevB.75.035115>.
- [33] Yang, H., Wang, B., Zhang, H., Shen, B., Li, Y., Wang, M., Wang, J., Gao, W., Kang, Y. & Li, L. (2023). Evolving cerundum nanoparticles at room temperature. *Acta Materialia* 205, 119038, 1-7. <https://doi.org/10.1016/j.actamat.2023.119038>.
- [34] Michaelson, H.B. (1977). The work function of the elements and its periodicity. *Journal of applied physics*. 48(11), 4729-4733. <https://doi.org/10.1063/1.323539>.
- [35] Schlesinger, R., Xu, Y., Hofmann, O.T., Winkler, S., Frisch, J., Niederhausen, J., Vollmer, A., Blumstengel, S., Henneberger, F. & Rinke, P. (2013). Controlling the work function of ZnO and the energy-level alignment at the interface to organic semiconductors with a molecular electron acceptor. *Physical Review B*. 87(15), 155311. <https://doi.org/10.1103/PhysRevB.87.155311>.
- [36] Liu, M., Jin, Y., Pan, J. & Leygraf, C. (2019). Co-Adsorption of H<sub>2</sub>O, OH, and Cl on aluminum and intermetallic surfaces and its effects on the work function studied by DFT calculations. *Molecules*. 24(23), 4284, 1-15. <https://doi.org/10.3390/molecules24234284>.
- [37] Golesorkhtabar, R., Pavone, P., Spitaler, J., Puschnig, P. & Draxl, C. (2013). ElaStic: A tool for calculating second-order elastic constants from first principles. *Computer Physics Communications*. 184(8), 1861-1873. <https://doi.org/10.1016/j.cpc.2013.03.010>.
- [38] de Jong, M., Chen, W., Angsten, T., Jain, A., Notestine, R., Gamst, A., Sluiter, M., Krishna Ande, C., van der Zwaag, S., Plata, J.J., Toher, C., Curtarolo, S., Ceder, G., Persson, K.A. & Asta, M. (2015). Charting the complete elastic properties of inorganic crystalline compounds. *Scientific Data*. 2(1), 150009, 1-13. <https://doi.org/10.1038/sdata.2015.9>.
- [39] Pugh, S. (1954). XCII. Relations between the elastic moduli and the plastic properties of polycrystalline pure metals. *The London, Edinburgh, and Dublin Philosophical Magazine and Journal of Science*. 45(367), 823-843. <https://doi.org/10.1080/14786440808520496>.
- [40] Shang, S., Wang, Y. & Liu, Z.-K. (2007). First-principles elastic constants of  $\alpha$ - and  $\theta$ -Al<sub>2</sub>O<sub>3</sub>. *Applied Physics Letters*. 90(10), 101909. <https://doi.org/10.1063/1.2711762>.
- [41] Candan, A., Akbudak, S., Uğur, Ş. & Uğur, G. (2019). Theoretical research on structural, electronic, mechanical, lattice dynamical and thermodynamic properties of layered ternary nitrides Ti<sub>2</sub>AN (A= Si, Ge and Sn). *Journal of Alloys and Compounds* 771, 664-673. <https://doi.org/10.1016/j.jallcom.2018.08.286>.
- [42] Sun, Z., Music, D., Ahuja, R. & Schneider, J.M. (2005). Theoretical investigation of the bonding and elastic properties of nanolayered ternary nitrides. *Physical Review B*. 71(19), 193402. <https://doi.org/10.1103/PhysRevB.71.193402>.
- [43] Mattis, S., Sang-Hyeok, L., Tobias, S., W.J. M. & Sandra, K.-K. (2023). Estimation of directional single crystal elastic properties from nano-indentation by correlation with EBSD and first-principle calculations. *Materials & Design*. 234, 112296, 1-15. <https://doi.org/10.1016/j.matdes.2023.112296>.
- [44] Fan, T., Ruan, Z., Zhong, F., Xie, C., Li, X., Chen, D., Tang, P. & Wu, Y. (2023). Nucleation and growth of L1<sub>2</sub>-Al<sub>3</sub>RE particles in aluminum alloys:A first-principles study. *Journal of Rare Earths*. 41(7), 1116-1126. <https://doi.org/10.1016/j.jre.2022.05.018>.
- [45] Liao, H.-c., Xu, H.-t. & Hu, Y.-y. (2019). Effect of RE addition on solidification process and high-temperature strength of Al- 12% Si- 4% Cu- 1.6% Mn heat-resistant alloy. *Transactions of Nonferrous Metals Society of China*. 29(6), 1117-1126. [https://doi.org/10.1016/S1003-6326\(19\)65020-X](https://doi.org/10.1016/S1003-6326(19)65020-X).
- [46] Belov, N. & Khvan, A. (2007). The ternary Al-Ce-Cu phase diagram in the aluminum-rich corner. *Acta Materialia*. 55(16), 5473-5482. <https://doi.org/10.1016/j.actamat.2007.06.009>.
- [47] Chen, Z., Chen, P. & Ma, C. (2012). Microstructures and mechanical properties of Al-Cu-Mn alloy with La and Sm addition. *Rare Metals*. 31, 332-335. <https://doi.org/10.1007/s12598-012-0515-6>.
- [48] Lang, J., Baer, Y. & Cox, P. (1981). Study of the 4f and valence band density of states in rare-earth metals. II. Experiment and results. *Journal of Physics F: Metal Physics* 11(1), 121. <https://doi.org/10.1088/0305-4608/11/1/015>.
- [49] Farahani, S.V., Veal, T.D., Mudd, J.J., Scanlon, D.O., Watson, G., Bierwagen, O., White, M., Speck, J.S. & McConville, C.F. (2014). Valence-band density of states and surface electron accumulation in epitaxial SnO<sub>2</sub> films.



- Physical Review B* 90(15), 155413. <https://doi.org/10.1103/PhysRevB.90.155413>.
- [50] Nogita, K., Yasuda, H., Yoshiya, M., McDonald, S., Uesugi, K., Takeuchi, A. & Suzuki, Y. (2010). The role of trace element segregation in the eutectic modification of hypoeutectic Al–Si alloys. *Journal of Alloys and Compounds*. 489(2) 415-420. <https://doi.org/10.1016/j.jallcom.2009.09.138>.
- [51] Jiajia, W., Kaixiao, Z., Guobing, Y., Jiangbo, C., Dan, S., Jinghua, J. & Aibin, M. (2023). Effects of RE (RE = Sc, Y and Nd) concentration on galvanic corrosion of Mg-Al alloy: a theoretical insight from work function and surface energy. *Journal of Materials Research and Technology*. 24, 6958-6967. <https://doi.org/10.1016/J.JMRT.2023.04.208>.